Journal of Materials Chemistry A

ROYAL SOCIETY OF CHEMISTRY

PAPER

View Article Online
View Journal | View Issue

Cite this: J. Mater. Chem. A, 2025, 13, 14229

Single-step electrodeposition of CNT/GO–Zn composites for enhanced stability in AFLBs†

Pooria Afzali, [abc] Eugenio Gibertini,[a] Saraswathy Venugopal[a] and Luca Magagnin [*a]

Although anode-free Li batteries (AFLBs) have the potential to provide high energy density, their practical use is hindered by challenges related to low coulombic efficiency, acceptable life cycle, and significant volume changes. Herein, zinc–carbon composites were electroplated on a Cu current collector. Both 1D (carbon nanotubes) and 2D (graphene oxide) nanostructured carbon particles were used as electroactive and stabilizing fillers to produce carbon nanotubes/Zn (CNT–Zn) and graphene oxide/Zn (GO–Zn) electrodes respectively. Lower concentrations of 0.01 g L^{-1} Graphene Oxide (GO) and Carbon Nanotubes (CNTs) in the precursor plating solution produced composite coatings that effectively mitigated local current density fluctuations, enhancing conductivity and the mechanical strength of the coating layer. In contrast, a 0.05 g L^{-1} concentration showed random CNT or GO aggregates. The Zn-composite electrodes demonstrated reduced plating resistance and volume expansion in half cells. Notably, the 0.01GO–Zn@Cu electrode exhibited a low nucleation overpotential. Additionally, there was an approximately 100% increase in cyclability, with an average Coulombic Efficiency (CE) above 95% for both 0.01GO–Zn@Cu and 0.01CNT–Zn@Cu cells compared to bare Cu and Zn@Cu. Full cells showed the same trend, significantly improving capacity retention and CE for composite-coated cells. GO exhibited superior electrochemical performance compared to CNTs by providing a more stable surface.

Received 3rd December 2024
Accepted 29th March 2025

DOI: 10.1039/d4ta08590f

rsc.li/materials-a

1. Introduction

The accelerated commercialization of lithium-ion batteries for energy storage systems can be attributed to their high volumetric energy density and gravimetric density. However, the burgeoning demand for Li-ion batteries is currently outpacing production capacities.[1] Achieving a volumetric energy density exceeding 1200 W h L^{-1} by 2030 appears to be a challenging prospect. Meeting this ambitious target will necessitate substantial advancements in battery technology and manufacturing processes to bridge the existing gap between demand and production.[2,3] Theoretical exploration of anode-free cell designs not only presents the potential for increased energy density but also signifies increased volumetric energy density and heightened safety. The absence of excess lithium on electrodes offers substantial advantages; however, it concurrently triggers rapid capacity decay in anode-free lithium metal batteries within just a few cycles of lithium plating/stripping.[4,5] This decay can be mainly attributed to the continuous consumption of lithium by the solid electrolyte interface (SEI) layer and the formation of dead lithium components, ultimately leading to a decline in cyclability over charge and discharge cycles.[6,7] Recently, diverse strategies have been explored to tackle the aforementioned challenges. These methods cover various aspects, including current collector engineering, which involves controlled Li-metal deposition through the design of deposition substrates, electrolyte engineering, the establishment of testing protocols, *etc.*[8,9] One of the significant barriers to complete trust in AFLBs remains safety concerns arising from potential volume changes at the negative electrode and uncontrolled Li dendrite growth.[10] Consequently, the investigation of modified Cu-based current collectors has been undertaken to achieve efficient and stable cycling, improved chemical stability of Li metal, enhanced lithiophilicity, and adhesion of Li plating during cycling.[11–13] These modifications encompass surface engineering (lithiophilic surface engineering), architectural design, using alloyed current collectors, and artificial Solid Electrolyte Interface (SEI) development. Notably, using lithiophilic thin film coatings are recognized as an effective and economical approach for modifying Cu current collectors.[14–16] Despite notable progress and growing interest in lithophilic coatings, which facilitate smoother lithium plating and subsequently reduce nucleation overpotentials during lithium plating with elements such as Zn,[17] Ag,[18] Au,[19] Sn,[20] *etc.*, limited research has been conducted on strengthening and sustaining lithophilic sites during plating and stripping

[a]Dipartimento di Chimica, Materiali e Ingegneria Chimica "Giulio Natta", Politecnico di Milano, Via Luigi Mancinelli 7, Milan 20131, Italy. E-mail: luca.magagnin@polimi.it
[b]Helmholtz Institute Ulm (HIU), Ulm D89081, Germany
[c]Karlsruhe Institute of Technology (KIT), Karlsruhe D76021, Germany

† Electronic supplementary information (ESI) available. See DOI: https://doi.org/10.1039/d4ta08590f

processes.[21–23] In this regard, zinc emerges as an appealing option as a lithiophilic agent due to its widespread availability and cost-effectiveness compared to other metals used in lithium alloying. When combined with lithium, zinc forms various intermetallic phases, leading to the creation of Li_xZn_y compounds. This alloy offers a relatively high volumetric capacity and facilitates promising chemical diffusion.[24–27] Additionally, the significant volume changes due to uneven deposition/plating and the "hostless" nature of the electrode cause continuous rupture and reformation of the solid electrolyte interphase (SEI) film, significant volume expansion leading to crack formation, and inadequate mechanical properties persist.[28] Furthermore, the accumulation of dead lithium, electrically isolated lithium enveloped by the solid electrolyte interphase (SEI), can impede lithium-ion transport in subsequent cycles, leading to heightened internal impedance and short circuits. Meanwhile, lithiophilic sites may detach or undergo structural alteration[29,30] Carbonaceous materials such as CNTs and graphene-like nanostructures, with their high electronic conductivity, minimal volume change, and large surface area, are promising for addressing challenges. Despite graphene oxide (GO) not being highly electrically conductive but ionically conductive,[31] it can prevent local electron buildup and distribute current density evenly.[32–35] It is reported that nickel sulfide nanoparticles were electrodeposited onto a CNT thin film, creating a paper-like composite known as NS@CNT, which led to an increase in specific capacity and cyclability.[36] A two-step sandwich coating of first Zn and then GO was applied to the Cu foil as the layered anode, with the GO acting as an artificial SEI layer with high ionic conductivity.[37] Another research study demonstrated that one-step electrodeposition of Sb/CNT composite films as the anode active material improved the mechanical and electrical connectivity of the electrode, resulting in extended cyclability for both Li and Na cells.[38] Additionally, there are other research studies regarding carbonaceous composites or layered structures of lithiophilic films for anode materials, utilizing different coating methods such as spin coating, CVD, and more, in various steps.[39–41] However, to our knowledge, comprehensive research on single-step co-electrodeposition of CNTs and GO with lithiophilic elements in different compositions for AFLBs has not yet been conducted.

In this work, we aimed to investigate the effect of various carbonaceous nanostructures, namely 1D carbon nanotubes (CNTs) and 2D graphene oxide (GO), when incorporated into a Zn coating to produce a carbon–Zn composite film on a Cu current collector through a simple one-pot electrodeposition process. The CNT and GO loadings in the CNT–Zn and GO–Zn composite coatings were tuned by adjusting the carbon nanoparticle concentrations (0.05 and 0.01 g L^{-1}) in the electroplating solution. The combined effects of lithiophilicity, improved electrode mechanical stability, and enhanced electroconductivity achieved using the Zn–CNT coatings, along with the improved uniform substrate network provided by the Zn–GO coatings, facilitated smoother lithium deposition compared to bare Cu. However, it was found that an excessive amount of CNTs and GO in the composite led to agglomeration in the electrodeposited coating, resulting in increased impedance and poorer electrochemical performance.

2. Experimental

2.1 Co-electrodeposition of CNT–Zn and GO–Zn composites on cu

The base zinc sulfamate solution was prepared according to our previously reported protocol [ref. 13]. Briefly, 2.43 M of sulfamic acid and 0.2 M of zinc carbonate basic were dissolved in water at 40 °C, and pH was finally adjusted at 3.3 by slowly adding NaOH. To properly pre-disperse CNTs in the zinc sulfamate solution, 5 ml of the zinc sulfamate solution was loaded in a ball milling jar with 0.08 g of polyvinylpyrrolidone (PVP, 40k, Merck) and different amounts of multi-walled carbon nanotubes (purity: >96%, outside diameter 8–10 nm, Nanografi), specifically 0.05 g or 0.01 g. Ball-milling was performed at 350 rpm for 30 min and finally the content was recovered and added to the rest of the zinc sulfamate solution to achieve a 0.05–0.01 g L^{-1} of CNT-dispersion. GO dispersions (GO, 1% wt, GO graphene) (0.05–0.01 g L^{-1}) were prepared by simply adding 0.08 g of PVP to 1 l of zinc sulfamate solution by stirring it for 1 h. Both the CNT and GO-loaded dispersions were sonicated by probe sonication (135 W, 60 min) before the electrodeposition process. The copper foil (10 μm thick) was soaked in a 0.03 M nitric acid solution for 30 seconds and then rinsed with water. Electrodeposition occurred at 24 mA cm^{-2} using a custom-built frame to hold the thin copper foil and a pure zinc strip as the counter electrode. The coated samples were rinsed with deionized water and subsequently dried using a stream of nitrogen gas. According to the carbon particle concentration in the electroplating solution, the final coatings were referred to as 0.01GO–Zn@Cu, 0.05GO–Zn@Cu, 0.01CNT–Zn@Cu, and 0.05CNT–Zn@Cu respectively while the reference pure zinc coating was referred to as Zn@Cu.

2.2 Cell assembling and electrochemical measurements

Electrochemical analyses were performed using CR 2032 coin cell assemblies in an Ar-filled glove box (O_2 level <0.5 ppm and H_2O level <0.5 ppm, MBraun) with a Celgard 2325 separator. For half cells, Li foil was used as the counter/reference electrode and coated Cu and bare Cu were used as the working electrodes. For full cells, coated and bare Cu as anodes and LFP as the cathode (NEI corp., areal capacity 1.25 mA h cm^{-2}) were used. The electrolyte (35 μL per cell) employed consisted of a 1 M lithium bis(trifluoromethane sulfonyl)imide (LiTFSI-Sigma Aldrich) salt dissolved in a 1 : 1 by-volume mixture of dioxolane and dimethoxyethane, with an additive of 0.3 M $LiNO_3$. Before any electrochemical measurements, all cells rested at an open circuit for 5 hours for stabilization. Cyclic voltammetry (CV) profiles were obtained with a scan rate of 0.5 mV s^{-1} within the voltage range of −0.2 V to 1 V *vs.* Li^+/Li using a Biologic VSP-300 potentiostat. Galvanostatic tests were conducted using a Neware BTS4000 battery tester, covering voltage ranges of −0.5 to 1 V for half cells and 3 to 4.3 V for full cells. Charge–discharge tests were carried out at ambient temperature. Furthermore,

electrochemical impedance spectroscopy (EIS) data were gathered using a sinusoidal voltage perturbation technique (Biologic VSP-300 potentiostat), with a 10 mV amplitude and frequency spanning from 4 MHz to 1 Hz. Before conducting EIS measurements, the open circuit potential (OCP) was also recorded for 60 minutes.

2.3 Structural characterization

SEM images were obtained using an EVO 50 EP microscope (Zeiss) at an accelerating voltage of 20 kV to examine the surface morphology of the prepared anode current collectors before cycling and after full lithium plating and stripping. Cell disassembly occurred in an Ar-filled glovebox, with salts and electrolyte residuals removed by washing samples with fresh dimethyl carbonate (DMC). X-ray energy dispersive spectrometry (EDS) analysis was conducted using an INCA x-sight detector (Oxford Instruments) to perform map analysis of the surface. Phase analysis was carried out using X-ray diffraction with a PW1830 instrument (Philips), employing Cu Kα1 radiation at 1.54058 Å. The thickness of the coated samples was determined using X-ray fluorescence (XRF, Fischer XAN-FD BC), with measurements conducted for 20 seconds at 10 different points on the surface of each electrode. X-ray photoelectron spectroscopy (XPS) analysis was performed using a Specs XPS system equipped with a Phoibos 150 energy analyzer. The measurements utilized monochromatized Al Kα radiation (300 W, 13 kV) with a pass energy of 30 eV for detailed scans. Binding energy calibration was referenced to the C 1s peak, either of conductive carbon additives (284.5 eV) or adventitious carbon (284.8 eV). To minimize surface contamination, samples were transported under an inert gas atmosphere to the XPS system's load lock. Peak fitting of the XPS data was carried out using CasaXPS software, employing Shirley-type backgrounds and Gaussian–Lorentzian (GL30) peak profiles.

3. Results and discussion

The thickness of the coated electrodes was ~1 μm with a uniform coverage on the whole plated area (typically 0.785 cm^2) as measured by XRF. The surface morphologies of all assembled electrodes were investigated by SEM and EDS. The bare copper foil surface (Fig. 1f) was rough, and the as-coated electrodes (Fig. 1a–e) exhibited a smoother but porous surface. Fig. 1a and b shows that low amounts of CNTs and GO (0.01 g L^{-1}) resulted in a more uniform and smoother coating for both the 0.01CNT–Zn@Cu and 0.01GO–Zn@Cu composite coatings. The Zn map of the 0.01 GO–Zn (Fig. 1b) electrode shows a more homogeneous and finely dispersed Zn coating similar to 0.01CNT–Zn@Cu as shown in Fig. 1a. Noteworthily, the carbon maps for both composite electrodes with a lower

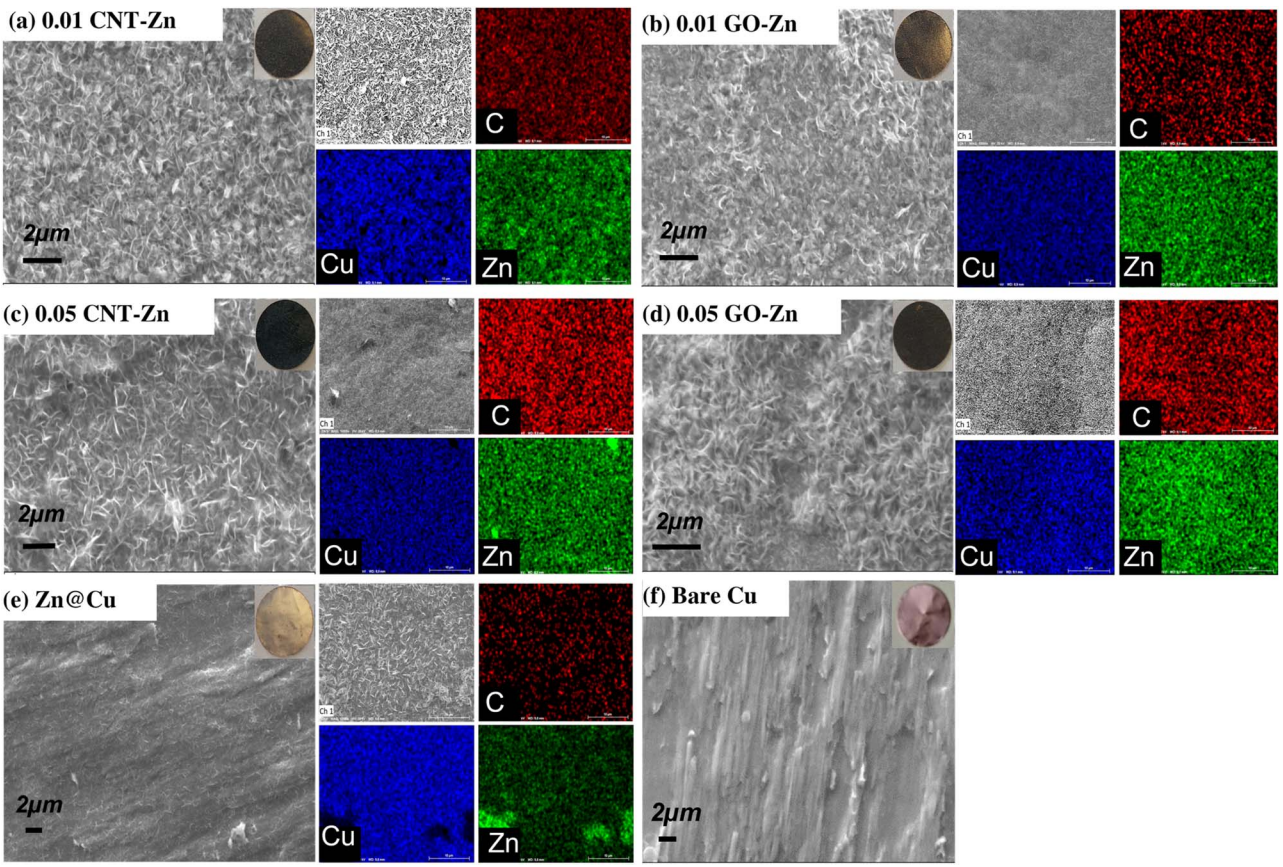

Fig. 1 SEM images and EDS maps of as-coated electrodes; (a) 0.01CNT–Zn@Cu. (b) 0.01GO–Zn@Cu. (c) 0.05CNT–Zn@Cu. (d) 0.05GO–Zn@Cu. (e) Zn@Cu. (f) SEM of bare Cu. The insets show pictures of the corresponding samples.

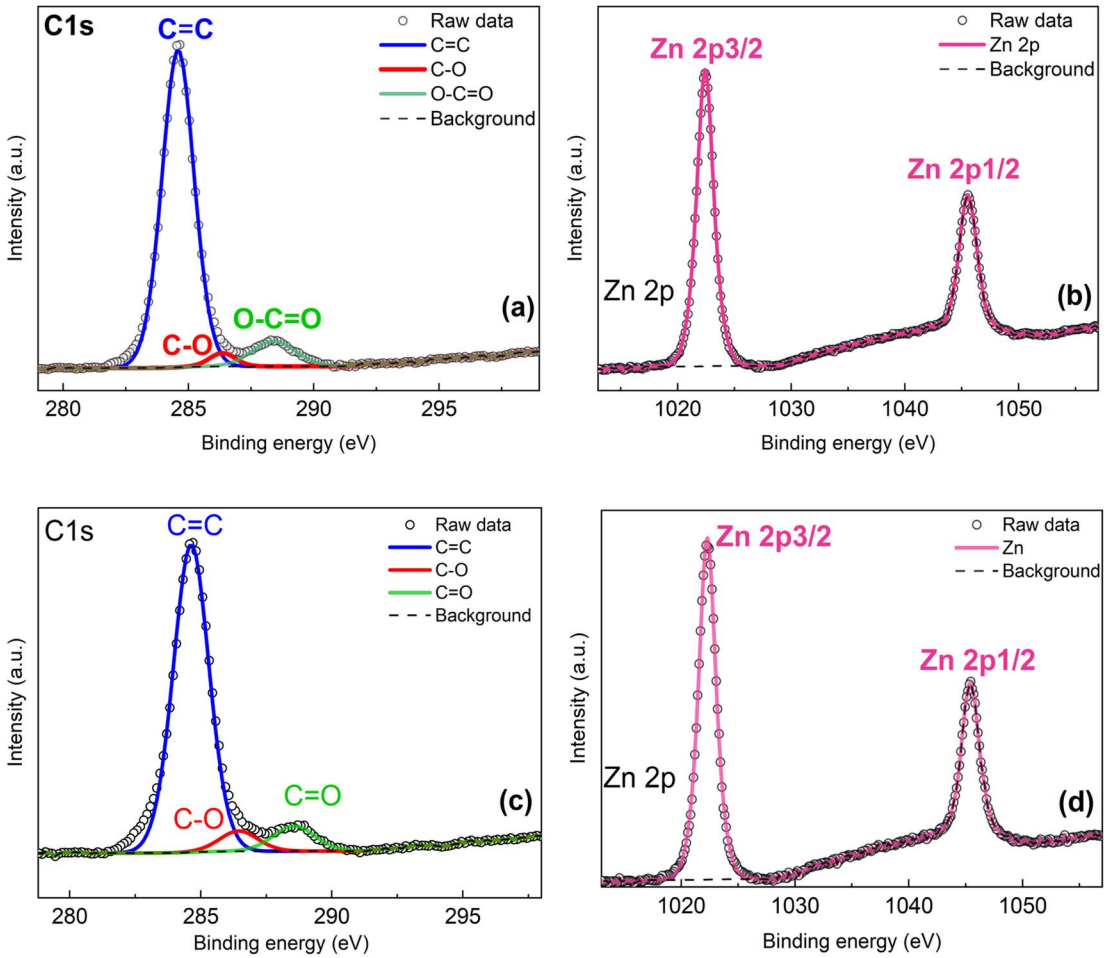

Fig. 2 XPS spectra of as-assembled electrodes: (a) C 1s in 0.01GO–Zn@Cu, (b) Zn 2p in 0.01GO–Zn@Cu, (c) C 1s in 0.01CNT–Zn@Cu, and (d) Zn 2p in 0.01CNT–Zn@Cu.

amount of carbon filler show less intensity and concentration in C compared with higher carbon content electrodes as shown in Fig. 1c and d. More importantly, by increasing the concentration of CNTs and GO from 0.01 g L^{-1} to 0.05 g L^{-1} in the CNT–Zn and GO–Zn composite coatings, we observed more irregularities in the surface morphology as clusters and clumps formed in the composite coating on the substrate. Both the 0.05CNT–Zn@Cu (Fig. 1c) and 0.05GO–Zn@Cu (Fig. 1d) composite-coated electrodes depict random aggregates, indicating the accumulation of carbonaceous particles with zinc and their uneven distribution. The Zn@Cu electrode exhibits relatively more uniform morphology compared to bare Cu, with corresponding zinc aggregates visible on the surface in its EDS images (Fig. 1e). The carbon-related signal reported in the EDS map of Zn@Cu might be attributed to the PVP in the Zn bath. The XRD plots of the coated Cu substrate by electrodeposition are shown in Fig. S1.† As observed, there is no evidence of carbon diffraction peaks, even at high concentrations of CNTs and GO in the plating bath (0.05 g L^{-1}). This suggests that the actual loading of carbon fillers in the coating is below the instrumental detection threshold (~3% wt). On the other hand, the Zn peaks were found at 36.26°, 39.01°, and 54.35° (JCPDS 00-004-0831, 98-024-7160); Cu peaks at 43.34° and 50.47° (JCPDS 98-062-7117 and 98-062-7113); and CuZn5 peaks at 37.60°, 42.05°, 57.64°, and 67.93° (JCPDS 00-035-1152).

Additionally, XPS analysis was conducted to investigate the elemental composition of the electrodes prepared at low carbon filler loading (Fig. 2). As shown in Fig. 2a (0.01GO–Zn@Cu) and Fig. 2c (0.01CNT–Zn@Cu), the C 1s peak at 284.5 eV corresponds to the formation of C=C bonds, accounting for 42.30 at% in 0.01GO–Zn@Cu and 46.90 at% in 0.01CNT–Zn@Cu. Peaks at 286.4 eV were attributed to C–O bonds, with 1.45 at% in 0.01GO–Zn@Cu and 3.34 at% in 0.01CNT–Zn@Cu. Moreover, the O–C=O bond (4.50 at%) was observed in 0.01GO–Zn@Cu, while the C=O bond (4.50 at%) was identified in 0.01CNT–Zn@Cu, both appearing at 288.6 eV. Fig. 2b,d show that the Zn 2p peak at 1022.3 eV corresponds to the Zn 2p3/2 in both the 0.01GO–Zn@Cu (13.90%) and 0.01CNT–Zn@Cu (12.74 at%) samples respectively. The XPS analysis reveals significant differences in the interaction of Zn with GO and CNTs. In Zn–GO, the higher Zn 2p signal and lower C 1s signal suggest stronger binding of Zn to the oxygen-containing functional groups, likely due to GO abundant carboxyl, hydroxyl, and epoxy groups.[42] This interaction may reduce the O–C=O signal, as

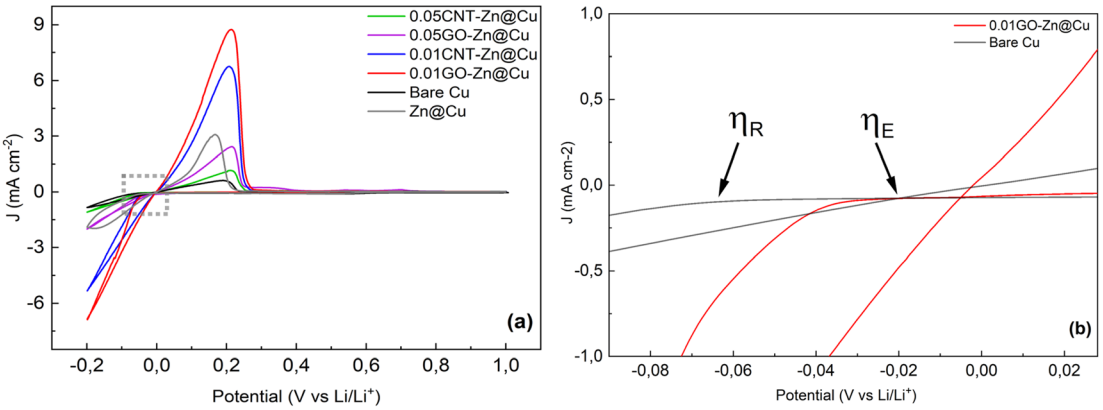

Fig. 3 (a). CV curves of the bare Cu foil, Zn@Cu, and composite coated electrodes at a scan rate of 0.5 mV s^{-1}; (b) the inset indicates the onset of nucleation for bare Cu and 0.01GO–Zn@Cu electrodes.

these groups bind with Zn or undergo partial reduction.[43] In Zn–CNTs, the weaker interaction leaves more C=O groups unaltered, resulting in a stronger signal.

The cyclic voltammetry plots (Fig. 3) depict the electrochemical behavior of the half cells, including bare Cu, Zn@Cu, and composite-coated electrodes, for the initial cycle, offering insight into the plating/stripping behavior. Alloy formation occurs between 0.4 V and 0 V. Beyond 0 V, a sharp increase in negative current density suggests lithium plating on the substrate. Then, upon sweeping the potential above 0 V, lithium metal is stripped from the electrode, with a broad peak at around 0.2 V indicating the Li stripping process. The sweep from −200 to 0 mV shows some linearity, suggesting a charge transfer kinetically controlled process through the charge transfer resistance. As a result, a simple ohmic relation can be applied for extracting plating resistance; larger slopes in this region denote lower plating resistance.[44] The composite coatings such as GO–Zn and CNT–Zn might enhance ionic and electron conductivity respectively, with the 0.01GO–Zn@Cu cell exhibiting the least ohmic behavior during plating. The enlarged section of the plot near 0 V shown in Fig. S2,† extracted from CV plots, indicates a reduction in nucleation overpotential for the coated samples, particularly those with lower carbon content. Also, Fig. 3b illustrates the potential differences between the bare Cu and GO1 electrodes. The potential difference between the equilibrium state (η_E) and the onset of reduction (η_R) can be attributed to the nucleation overpotential as $\eta = \eta_R - \eta_E$.[45–47] Reported values of the nucleation overpotential by CV are depicted in Table 1. The η increased with the addition of CNTs and GO in the composites. The highest values were observed for Zn@Cu and bare Cu, with 41.8 mV and 44.41 mV, respectively.

High nucleation barriers and unsuitable hosts for lithium nucleation cause dendritic lithium growth. This growth is accompanied by the continuous breaking and reforming of the solid electrolyte interphase (SEI) during the stripping and plating processes. Consequently, a porous lithium structure forms, which includes electronically isolated or "dead" lithium. This thick, poorly conductive lithium increases plating resistance and consumes active lithium in subsequent cycles, leading to the degradation of the electrochemical cell.

The phases for the 0.01GO–Zn@Cu electrode were analyzed by XRD both in the incipient growth regime and fully stripped state, as shown in Fig. S3a.† As shown in Fig. S3b,† the XRD patterns relative to the GO–Zn composite coating in the incipient Li growth regime revealed the presence of lithium-containing phases such as the Li_1Zn_1 alloy (JPCDS 98-010-4792), Cu (JPCDS 00-003-1005) and dilithium oxide (JPCDS 98-018-2025). After stripping, the 0.01GO–Zn@Cu electrode (Fig. S3c†) showed intense Zn peaks (JPCDS 00-004-0831) and Cu peaks (JPCDS 98-067-0771) only. No metallic lithium peaks were detected after stripping, indicating that the stripping and dealloying process was complete. During plating, lithium could alloy with the coated substrate to form a Li–Zn alloy. In order to investigate the Li growth orientation after full plating on bare Cu and 0.01GO–Zn@Cu electrodes, plating was performed at a higher capacity of 2 mA h cm^{-2} to ensure that the lithium peak could be detected. As shown in Fig. S4,† Li peaks at ∼36° and ∼64° (2θ) were observed for both electrodes, indicating that the deposited lithium has similar crystallographic orientation on both substrates.

The surface morphologies of all electrodes after Li plating and after Li stripping were investigated by SEM. During discharging, lithium was plated onto bare electrodes, zinc-modified electrodes, and zinc composite electrodes, resulting in various lithium morphologies, as depicted in Fig. 4a–l. Both bare Cu (Fig. 4f) and Zn@Cu (Fig. 4e) electrodes exhibit nonuniform, loose, and porous lithium deposition even with

Table 1 Electrochemical parameters of nucleation overpotential extracted by cyclic voltammetry at 0.5 mV s^{-1}

	0.01GO–Zn@Cu	0.01CNT–Zn@Cu	0.05GO–Zn@Cu	0.05CNT–Zn@Cu	Zn@Cu	Bare Cu
η (mV)	25.26	27.49	33.42	37.2	41.8	44.41

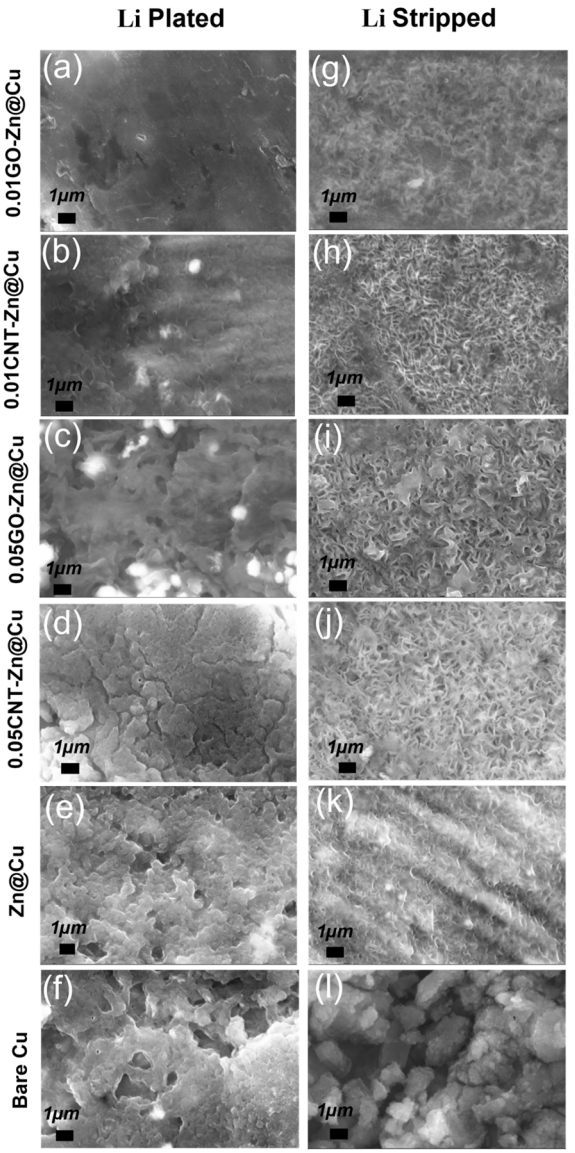

Fig. 4 SEM images of Li-plated electrodes; (a) 0.01GO–Zn@Cu; (b) 0.01CNT–Zn@Cu; (c) 0.05GO–Zn@Cu; (d) 0.05CNT–Zn@Cu; (e) Zn@Cu; (f) bare Cu. SEM images of Li-fully stripped electrodes; (g) 0.01GO–Zn@Cu; (h) 0.01CNT–Zn@Cu; (i) 0.05GO–Zn@Cu; (j) 0.05CNT–Zn@Cu; (k) Zn@Cu; (l) bare Cu.

cracks on the lithium plated electrode due to the high localized current density. Plating on bare copper shows small lithium particles clustering near larger ones, with a visible growth in the size of the initial nuclei on the copper surface, and large dendritic structures accumulated on top of each other. The Zn@Cu electrode demonstrates a slightly more uniform deposition compared to bare Cu, although it still shows dendritic structures, but smaller in size. The 0.05CNT–Zn@Cu (Fig. 4d) and 0.05GO–Zn@Cu (Fig. 4c) samples exhibit fewer dendrites and more lithium covered surfaces interspersed with dense and less porous regions, attributed to the agglomerated morphology of the substrate before Li plating and no cracks observed for the 0.05GO–Zn@Cu electrode. In contrast, the 0.01CNT–Zn@Cu (Fig. 4b) and 0.01GO–Zn@Cu (Fig. 4a) samples, containing a lower amount of carbonaceous active material, show uniform Li deposition with a dense and compact structure. It appears that 0.01GO–Zn@Cu is better at dissipating localized current density and providing an interconnected, flat lithium layer, even more uniform than that on the 0.01CNT–Zn@Cu electrode. This may be attributed to the stable formation of the SEI and uniform nucleation/growth of Li on the substrate. After the stripping stage, no clear lithium spots were observed on the surface of the 0.01CNT–Zn@Cu (Fig. 4h) and 0.01GO–Zn@Cu (Fig. 4g) electrodes, indicating potentially higher coulombic efficiency during cycling. However, some residual lithium was evident on the substrate, particularly on bare Cu (Fig. 4l), accompanied by a damaged SEI layer. Dendritic remnants of lithium were observed on both 0.05CNT–Zn@Cu (Fig. 4j) and 0.05GO–Zn@Cu (Fig. 4i) electrodes indicating incomplete stripping. The Zn@Cu electrode (Fig. 4k) also exhibited a rough surface including high remaining lithium spots.

To investigate the potential effect on SEI formation of carbon contained in the composite electrodes, XPS analyses were performed after lithium plating. In particular, Fig. 5 presents the XPS analysis concerning the F 1s and C 1s region for three electrode samples: Fig. 5a (bare Cu), Fig. 5b and c (0.01CNT–Zn@Cu), and Fig. 5d and e (0.01GO–Zn@Cu). The F 1s spectra in all samples display two characteristic peaks: LiF at 685.2 eV and CF_3 at 688.5 eV. The summary in Fig. 5f quantifies the LiF and CF_3 atomic content for each electrode, along with their intensity ratio (I_{LiF}/I_{CF_3}). For the bare Cu electrode (Fig. 5a), the SEI contained 5.58 at% LiF and 4.10 at% CF_3, yielding an I_{LiF}/I_{CF_3} ratio of 1.36. In contrast, the 0.01CNT–Zn@Cu electrode (Fig. 5b) showed a higher LiF content (10.51 at%) and increased CF_3 (5.58 at%), leading to an I_{LiF}/I_{CF_3} ratio of 1.88. The most significant increase in LiF content was observed in the 0.01GO–Zn@Cu electrode (Fig. 5d), where LiF reached 15.20 at%, while CF_3 decreased to 2.31 at%. This resulted in the highest I_{LiF}/I_{CF} ratio of 6.58, indicating the preferential decomposition of LiTFSI into LiF rather than CF_3. The increased LiF content in the modified electrodes, especially in the 0.01GO–Zn@Cu electrode, suggests that the composite substrate significantly influenced SEI formation. LiF is known for its strong adhesion to the electrode surface, leading to a robust and dense SEI layer. It also enhances Li^+ ion diffusivity and reduces surface resistance due to its wide electrochemical stability window. The high LiF ratio in 0.01GO–Zn@Cu implies that the graphene oxide–zinc composite promoted the reduction of the $TFSI^-$ anion on the lithium metal surface, facilitating rapid Li^+ diffusion while preventing electron transfer at the interface.[48,49] This mechanism helped inhibit Li dendrite growth and minimizing SEI thickness accumulation over cycling. The C 1s spectra further revealed differences in SEI composition. Both composite-coated electrodes exhibit notable carbon spectra. The 0.01CNT–Zn@Cu electrode (Fig. 5c) primarily displays a C=C peak at 284.5 eV (32.24 at%), along with C–O (3.31 at%), C=O (2.40 at%), and CF_3 (2.02 at%). Meanwhile, the 0.01GO–Zn@Cu electrode (Fig. 5e) showed a stronger C=C signal at 284.6 eV (46.12 at%), with C–O (4.34 at%), O–C=O (2.51 at%), and a minimal CF_3 contribution (0.44 at%). The lower CF_3 content in GO–Zn@Cu is consistent with its

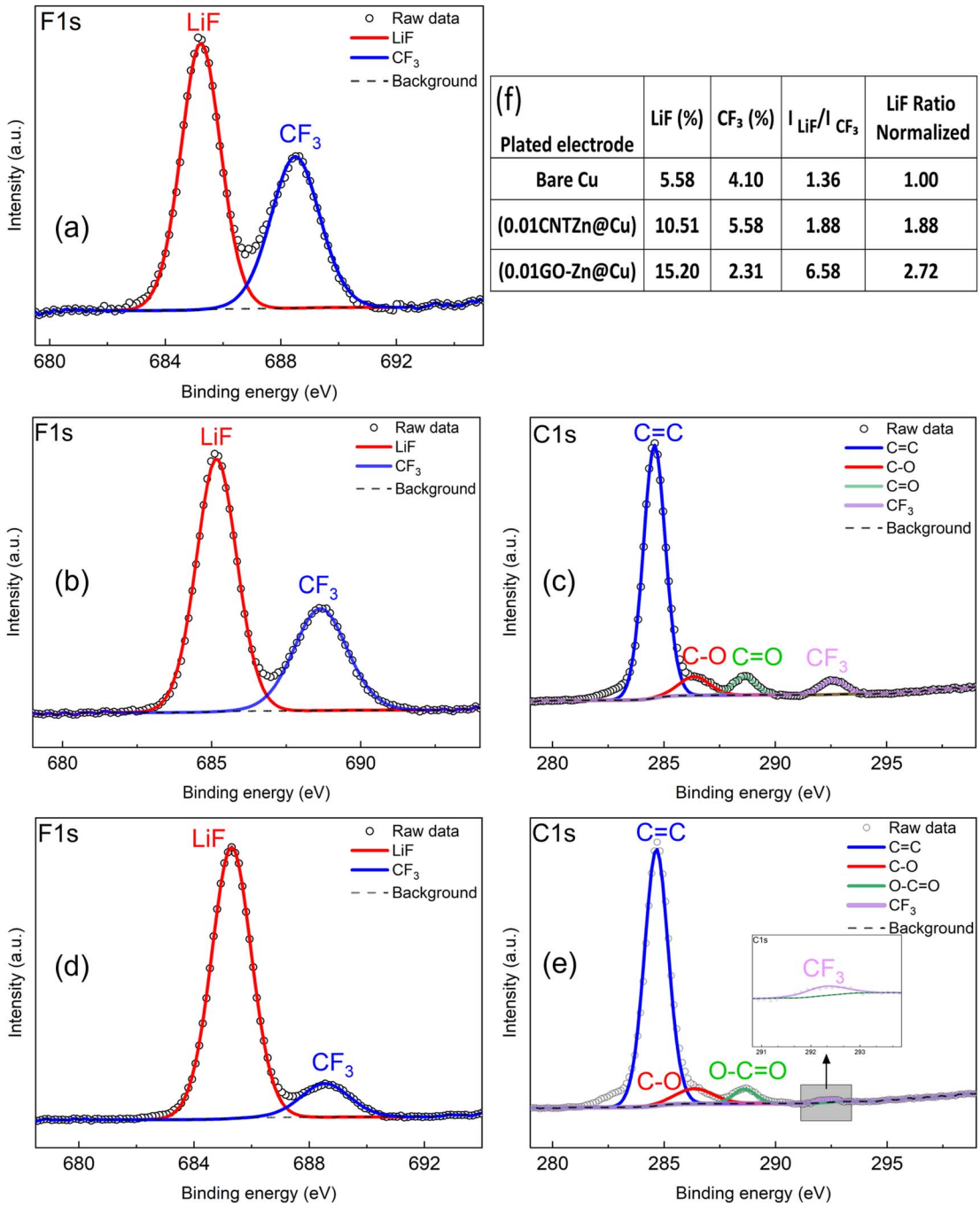

(f) Plated electrode	LiF (%)	CF_3 (%)	I_{LiF}/I_{CF_3}	LiF Ratio Normalized
Bare Cu	5.58	4.10	1.36	1.00
(0.01CNTZn@Cu)	10.51	5.58	1.88	1.88
(0.01GO-Zn@Cu)	15.20	2.31	6.58	2.72

Fig. 5 XPS analysis of SEI composition after lithium plating: F 1s spectra for (a) bare Cu, (b) 0.01CNT–Zn@Cu, and (d) 0.01GO–Zn@Cu; C 1s spectra for (c) 0.01CNT–Zn@Cu and (e) 0.01GO–Zn@Cu. (f) The summary table presents LiF and CF_3 content, their intensity ratio, and the normalized LiF ratio.

higher LiF ratio, reinforcing the idea that 0.01GO–Zn@Cu promotes LiTFSI decomposition into LiF, leading to a more effective SEI layer with superior ionic transport properties.[50,51] These findings highlight that composite-coated electrodes, particularly 0.01GO–Zn@Cu, significantly alter SEI composition by enhancing LiF formation. This results in a denser, more stable SEI that facilitates Li^+ transport while suppressing dendrite growth, ultimately improving the cycling performance of lithium metal anodes.

For a more profound understanding of Li deposition progression, it's essential to evaluate the lithiophilic properties of the substrate by measuring and analyzing nucleation overpotential. This overpotential refers to the voltage difference between the lowest point and the plateau potential value.[52,53] As illustrated in Fig. 6a a high overpotential of 76.8 mV for the bare Cu at 0.5 mA cm^{-2} indicates the low lithiophilicity of the substrate. In contrast, the Zn coated electrode showed a nucleation overpotential of 60.7 mV and for the 0.05CNT–Zn@Cu,

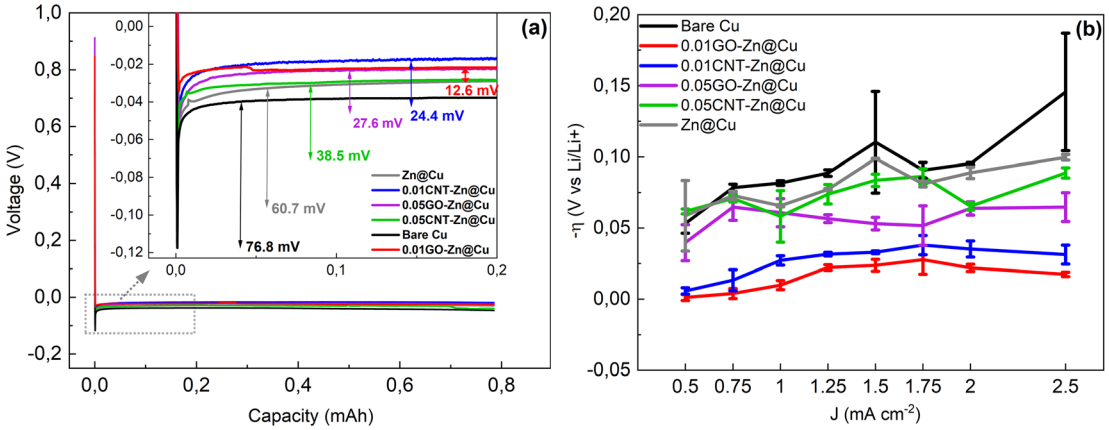

Fig. 6 (a) Half-cell discharge curves of all cells at 0.5 mA cm^{-2}; the inset shows the Li nucleation region of the cells. (b) The Li nucleation overpotential for all cells at different current densities.

0.05GO–Zn@Cu, 0.01CNT–Zn@Cu and 0.01GO–Zn@Cu electrodes, it was estimated to be 38.5 mV, 27.6 mV, 24.4 mV and 12.6 mV respectively. The low nucleation overpotentials (η) observed in the GO–Zn composites suggest a larger electroactive surface area, which results in reduced local current density and facilitates the creation of favorable nucleation sites for lithium. Additionally, GO has a large specific surface area that may be helpful in the structural stabilization of Zn upon alloying. On the other hand, CNTs provide high electronic conductivity and can improve ion insertion and extraction. Both the CNT–Zn and GO–Zn composites mitigate excessive cracking of the Zn substrate during lithiation and play a beneficial role in managing dendrite growth, minimizing volume fluctuations and maintaining SEI stability.[54] However, an increased amount of both GO and CNTs may lead to surface agglomeration, resulting in decreased uniformity of nucleation sites for Li. Undoubtedly, the applied current density plays a crucial role in the lithium deposition behavior and overpotential of the cell in AFLMs. To investigate the influence of current density on nucleation overpotential, the plating/stripping current density was adjusted within the range of 0.5 to 2.5 mA cm^{-2}, as illustrated in Fig. 6b. The average overpotentials of three cycles for each cell have been recorded. Both 0.01CNT–Zn@Cu and 0.01GO–Zn@Cu electrodes exhibit the lowest nucleation overpotential, and at various C-rates, there are minimal fluctuations in overpotential. Conversely, other electrodes display higher overpotentials and significant fluctuations at different current densities. Notably, bare Cu and Zn substrates exhibit a considerable increase in overpotential at higher current densities compared to other electrodes. The consistent and uniform low nucleation overpotential observed in 0.01CNT–Zn@Cu and 0.01GO–Zn@Cu electrodes under different conditions suggests that the substrate surfaces remain homogeneous after multiple cycles. This indicates their ability to withstand volume expansions, and it implies a stronger (SEI) layer and uniform Li deposition and alloying with Zn.

The coulombic efficiency (CE) of the half cells cycled at 0.5 mA cm^{-2} with an areal capacity of 1 mA h cm^{-2} is depicted in Fig. 7a. Bare Cu exhibited persistently low CE, remaining below 95% throughout its lifespan and sustaining only 94 cycles above

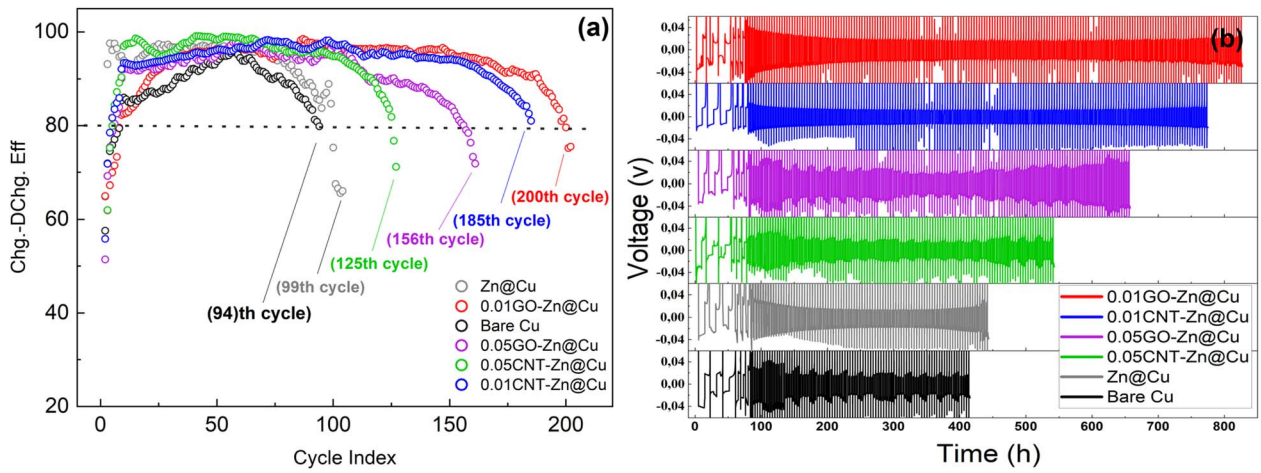

Fig. 7 (a) Coulombic efficiencies (CE%) of plating/stripping tests with a threshold line of 80%. (b) Galvanostatic long cycling curves of the half-cells.

80%. Notably, a sharp decline in CE% began after the 60th cycle. Conversely, the Zn@Cu cell demonstrated higher initial CE and lasted for 99 cycles with CE exceeding 85%. The 0.05CNT–Zn@Cu, 0.05GO–Zn@Cu, 0.01CNT–Zn@Cu, and 0.01GO–Zn@Cu electrodes could maintain CE above 90% for 125, 156, 185, and 200 cycles, respectively. Following an initial increase in CE% during the initial cycles, the 0.01CNT–Zn@Cu and 0.01GO–Zn@Cu electrodes could sustain CE > 95% for around 155 and 167 cycles, respectively demonstrating an excellent reversible plating/stripping. Additionally, the 0.01CNT–Zn and 0.01GO–Zn composite electrodes exhibited a stable SEI layer due to the higher mechanical strength of the uniform composite substrate, along with accommodating high-volume expansion, which contributes to their excellent CE performance.[55] In contrast, the fluctuating CE observed in bare Cu and Zn cells can be ascribed to the formation of mossy Li and sporadic reconnection of the thickened SEI layer.[56] Fig. 7b demonstrates the continuous voltage profiles of the cycled half cells. The cells underwent cycling at 0.1 mA cm^{-2} for three cycles, followed by three cycles at 0.25 mA cm^{-2}, aiming to stabilize them and facilitate the formation of a SEI layer. Subsequent cycles at 0.5 mA cm^{-2} continued until the cell degraded. The fluctuating voltage hysteresis observed during Li-plating/stripping on the bare Cu substrate was caused by the unstable interface between Li and the bare Cu. The cycling life was relatively short, lasting less than 96 cycles (415 hours). Zn@Cu, 0.05CNT–Zn@Cu, and 0.05GO–Zn@Cu cells were able to maintain 99 cycles (443 hours), 126 cycles (543 hours), and 158 cycles (658 hours) respectively. The overpotential displayed hysteretic increases, indicating that upon extended cycling the internal cell resistance increased, reflecting severe solid electrolyte interphase (SEI) growth and the accumulation of dead lithium. In contrast, the low carbonaceous zinc composites of 0.01CNT–Zn@Cu and 0.01GO–Zn@Cu exhibited a relatively smooth voltage plateau and high cyclability for 775 hours (185 cycles) and 830 hours (200 cycles) respectively. This confirms the homogeneous Li^+ flux and likely improved mechanical stability of these Zn composite electrodes where the evenly distributed carbon nanoparticles in the Zn matrix were likely able to mitigate the cracking and pulverization of Zn resulting from the volume expansion during the Zn_xLi_y alloy formation and consecutive plating/stripping.

It is crucial to develop a clear understanding of the impedance characteristics of the solid electrolyte interphase (SEI) layer and the evolution of impedance data during the Li plating–stripping processes. Electrochemical Impedance Spectroscopy (EIS) analysis was performed on the half cells charged at 1 V in a fully stripped state. The Nyquist plots for cycles 1st, 5th, and 10th are depicted in Fig. 8, along with their corresponding equivalent circuit for the charge transfer (R_{ct}), and the

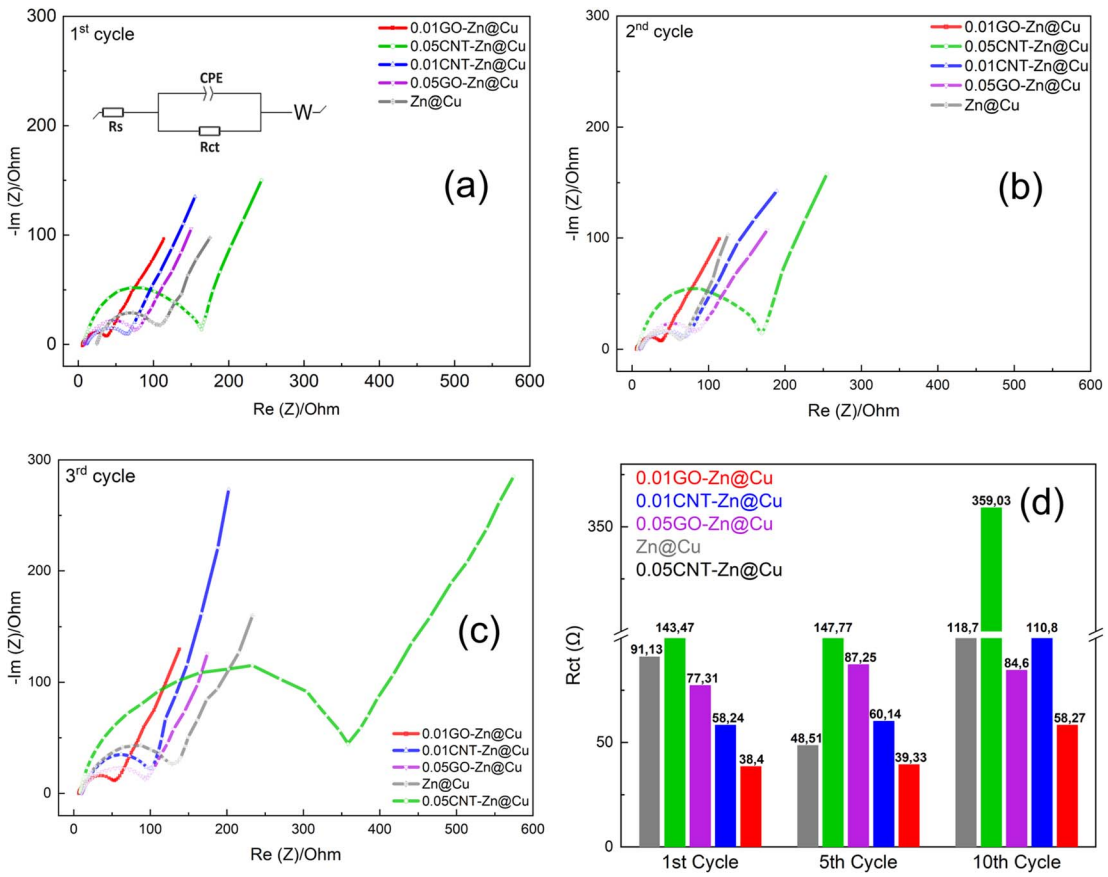

Fig. 8 EIS spectra of the half cells after being fully stripped at 1 V at different cycles. (a) After the 1st cycle (inset shows the equivalent circuit model of half-cells). (b) After the 5th cycle and (c) after the 10th cycle. (d) Reported charge transfer (R_{ct}) values.

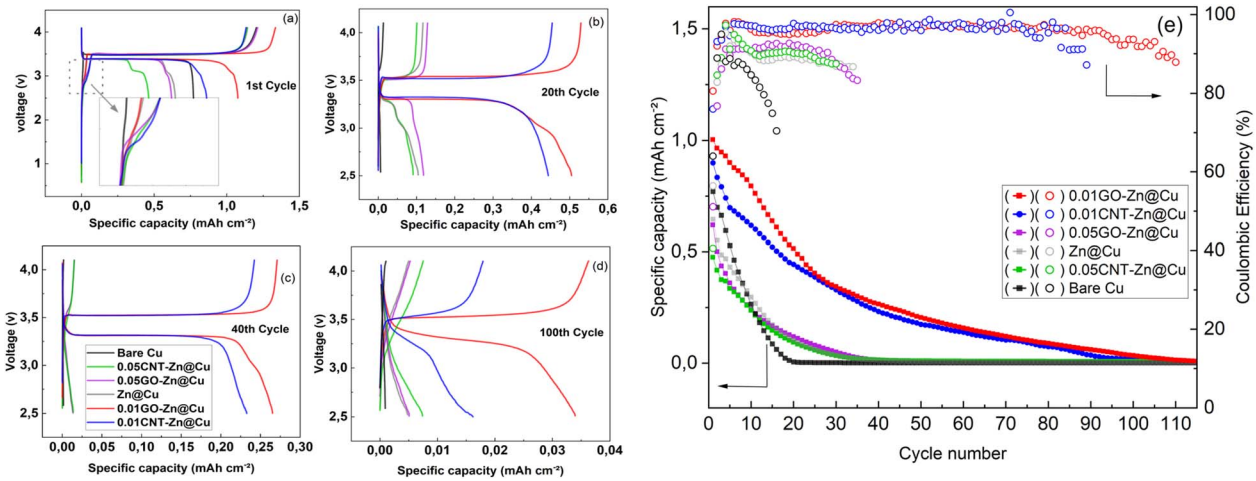

Fig. 9 (a) Voltage profiles of the anode-free LFP||modified-Cu full cell for different cycles; (a) 1st cycle and the inset shows a distinct new plateau around 3 V, indicating the transfer of active Li. (b) 20th cycle. (c) 40th cycle. (d) 100th cycle. (e) Extended cycling performance of the anode-free LFP||modified-Cu full cells indicating capacity retention and CE%.

fitted plots and values are shown in Fig. S5.† The semi-circles observed in the Nyquist plot indicate impedance for Li^+ transport across the electrode surface, denoted as charge transfer resistance R_{ct}, in high-frequency ranges. The equivalent circuit model is used to approximate the cell resistor (R_s) connected to a constant phase element (CPE) and a charge transfer resistor (R_{ct}) in parallel with a Warburg element (W). In general, impedance data for all samples increased in subsequent cycles compared to the first cycle. This can be attributed to continuous SEI thickening and decomposition, which affects the transmission of Li^+ ions.[57] However, as seen in Fig. 8e during the first cycle, when the SEI is forming, the 0.01GO–Zn@Cu and 0.01CNT–Zn@Cu composite interfaces exhibited R_{ct} values of 38.4 Ω and 58.24 Ω at first, sensibly lower than that of Zn@Cu (91.13 Ω). Also, the R_{ct} of the Zn@Cu (118.7 Ω) electrode was 103.8% more than that of 0.01GO–Zn@Cu (58.27 Ω) in the 10^{th} cycle. Furthermore, Zn@Cu and 0.05CNT–Zn@Cu cells exhibited the highest average R_{ct} values throughout all cycles. This can be attributed to the gradual failure and loss of the active material layer on the substrate, as evidenced by SEM images captured after plating and stripping (Fig. 4).[58]

To further assess the electrochemical performance of AFLBs, LFP|Cu full cells with various coatings were assembled and cycled within a voltage range of 2.5 to 4.1 V. Specific capacities in different cycles are depicted in Fig. 9a–d. The full cells with 0.01CNT–Zn@Cu and 0.01GO–Zn@Cu electrodes displayed the least capacity loss over 100 cycles. Fig. 9a illustrates the first cycle voltage profile of full cells. Relative to bare Cu, all other electrodes exhibited a distinct new plateau around 3 V, indicating the transfer of active Li from the LFP cathode to the anode as a Li reservoir, thereby resulting in higher charge capacities due to the Li and Zn alloying. Furthermore, based on the charge–discharge profiles in the 1st, 20th, 40th, and 100th cycles as shown in Fig. 9a–d, it is evident that there is no apparent increase in polarization or significant voltage drop observed during the subsequent cycling processes for 0.01GO–Zn@Cu and 0.01CNT–Zn@Cu electrodes. So, degradation and capacity loss primarily resulted from the depletion of lithium inventory and dead lithium formation. This phenomenon is particularly pronounced in the bare Cu, Zn@Cu, 0.05GO–Zn@Cu, and 0.05CNT–Zn@Cu electrodes. In contrast, the 0.01GO–Zn@Cu electrode demonstrated the highest initial specific capacity of 1 mA h cm^{-2}, with a capacity retention of approximately 51.3%, 26.42%, and 3.38% after 20, 40, and 100 cycles, respectively, and a CE of around 96% over 100 cycles (Fig. 9e). This performance is consistent with the cycling performance of half-cells. Similarly, the 0.01CNT–Zn@Cu battery retained about 49.38%, 25.85%, and 1.79% of its initial capacity after 20, 40, and 100 cycles, respectively, also maintaining a high CE of approximately 96% over 100 cycles. In contrast, the bare Cu, Zn@Cu, 0.05CNT–Zn@Cu, and 0.05GO–Zn@Cu electrodes exhibited much lower capacity retentions with significantly lower CE% and faster capacity decay. The excellent capacity retention and CE of the 0.01GO–Zn@Cu and 0.01CNT–Zn@Cu full cells highlighted the crucial role of loading carbon nanostructures in the Zn matrix. In particular, the even distribution of GO and CNTs, when added in low amounts in the plating solution, helped prevent local current density fluctuations and enhance the mechanical strength of the coating layer. These uniform coatings lead to more consistent lithium plating deposition, inhibit dendritic growth, and accelerate the kinetics of electrochemical reactions, demonstrating the proposed one-step composite electrodeposition approach as a promising technique to achieve suitable anodic electrodes for AFLBs.

4. Conclusions

In this work, CNTs and GO were used as carbon nanofillers and incorporated into a Zn matrix by a fast and easy direct electroplating method, to achieve a zinc–carbon composite thin coating on Cu collector foil. The proposed approach aimed to enhance the anode stability in AFLBs. The composite electrodes, CNT–Zn@Cu and GO–Zn@Cu, improved Li wettability through Zn–Li alloying while boosting mechanical strength by mitigating excessive cracking of the Zn substrate during

lithiation thanks to the carbonaceous nanofillers. This innovative composition combines multiple benefits to achieve highly reversible, stable, and non-dendritic Li plating and stripping. The optimal composite coating, 0.01GO–Zn@Cu, significantly reduced the nucleation overpotential compared to the bare Cu anode. It also maintained a coulombic efficiency above 95% for 167 cycles at 0.5 mA cm^{-2}, demonstrating superior stability over bare Cu electrodes and thin Zn coatings in half cells. Furthermore, the R_{ct} values for 0.01GO–Zn@Cu and 0.05CNT–Zn@Cu were the lowest at 38.40 Ω and 58.24 Ω, respectively, after the first cycle and remained the lowest also in the 5th and 10th cycles compared to the other coated electrodes. This indicates higher Li^+ reaction kinetics likely due to the improved structural stability of the coatings, owing to the presence of the carbonaceous filler, and lower extent of SEI accumulation. The LFP‖0.01GO–Zn@Cu full cell performance was the highest with a capacity retention of approximately 51.3% and 26.42%, after 20 and 40 cycles, respectively, and a high coulombic efficiency (CE) of around 96% over 100 cycles. The XPS analysis shows that the 0.01GO–Zn@Cu electrode contains approximately 2.7 times more LiF in the SEI compared to the bare Cu electrode. Lower concentrations of 0.01 g L^{-1} of Graphene Oxide (GO) and Carbon Nanotubes (CNTs) were found to effectively mitigate local current density fluctuations and improve the mechanical stability of the coating layer, in comparison to a composite coating electrode with a concentration of 0.05 g L^{-1}. The 0.05 g L^{-1} CNT or GO coatings displayed either non-uniform or aggregated coatings. In general, this work demonstrates the direct electrodeposition of lithiophilic metal composites as a viable strategy for improved Li plating reversibility.

Data availability

The data supporting this article have been included as part of the ESI.†

Author contributions

Pooria Afzali: writing – original draft, supervision, methodology, investigation, formal analysis, data curation, conceptualization. Eugenio Gibertini: original draft, methodology, investigation, formal analysis, conceptualization. Saraswathy Venugopal: methodology, investigation. Luca Magagnin: writing – original draft, validation, supervision, resources, project administration, methodology, conceptualization.

Conflicts of interest

There are no conflicts to declare.

Acknowledgements

The authors thank Dr Jian Wang and Dr Thomas Diemant for their helpful discussions at the Helmholtz Institute Ulm (HIU).

References

1 J. He, J. Meng and Y. Huang, Challenges and recent progress in fast-charging lithium-ion battery materials, *J. Power Sources*, 2023, **570**, 232965, DOI: 10.1016/j.jpowsour.2023.232965.
2 M. Winter, B. Barnett and K. Xu, Before Li Ion Batteries, *Chem. Rev.*, 2018, **118**, 11433–11456, DOI: 10.1021/acs.chemrev.8b00422.
3 F. Duffner, N. Kronemeyer, J. Tübke, J. Leker, M. Winter and R. Schmuch, Post-lithium-ion battery cell production and its compatibility with lithium-ion cell production infrastructure, *Nat. Energy*, 2021, **6**, 123–134, DOI: 10.1038/s41560-020-00748-8.
4 Y. Tian, Y. An, C. Wei, H. Jiang, S. Xiong, J. Feng and Y. Qian, Recently advances and perspectives of anode-free rechargeable batteries, *Nano Energy*, 2020, **78**, 10534, DOI: 10.1016/j.nanoen.2020.105344.
5 C.-Y. Park, J. Kim, W.-G. Lim and J. Lee, Toward Maximum Energy Density Enabled by Anode-Free Lithium Metal Batteries, *Recent Progress and Perspective toward Maximum Energy Density Enabled by Anode-free Recent Progress and Perspective*, 2023, DOI: 10.22541/au.167938208.83944769/v1.
6 S. Liu, K. Jiao and J. Yan, Prospective strategies for extending long-term cycling performance of anode-free lithium metal batteries, *Energy Storage Mater.*, 2023, **54**, 689–712, DOI: 10.1016/j.ensm.2022.11.021.
7 H. Xu, C. Han, W. Li, H. Li and X. Qiu, Quantification of lithium dendrite and solid electrolyte interphase (SEI) in lithium-ion batteries, *J. Power Sources*, 2022, **529**, 231219, DOI: 10.1016/j.jpowsour.2022.231219.
8 Z. Xie, Z. Wu, X. An, X. Yue, J. Wang, A. Abudula and G. Guan, Anode-free rechargeable lithium metal batteries: Progress and prospects, *Energy Storage Mater.*, 2020, **32**, 386–401, DOI: 10.1016/j.ensm.2020.07.004.
9 C. Heubner, S. Maletti, H. Auer, J. Hüttl, K. Voigt, O. Lohrberg, K. Nikolowski, M. Partsch and A. Michaelis, From Lithium-Metal toward Anode-Free Solid-State Batteries: Current Developments, Issues, and Challenges, *Adv. Funct. Mater.*, 2021, **31**, 2106608, DOI: 10.1002/adfm.202106608.
10 B. T. Heligman, K. J. Kreder and A. Manthiram, Zn-Sn Interdigitated Eutectic Alloy Anodes with High Volumetric Capacity for Lithium-Ion Batteries, *Joule*, 2019, **3**, 1051–1063, DOI: 10.1016/j.joule.2019.01.005.
11 G. Lai, J. Jiao, C. Fang, Y. Jiang, L. Sheng, B. Xu, C. Ouyang and J. Zheng, The Mechanism of Li Deposition on the Cu Substrates in the Anode-Free Li Metal Batteries, *Small*, 2023, **19**, 220541, DOI: 10.1002/smll.202205416.
12 C. H. Jo, K. S. Sohn and S. T. Myung, Feasible approaches for anode-free lithium-metal batteries as next generation energy storage systems, *Energy Storage Mater.*, 2023, **57**, 471–496, DOI: 10.1016/j.ensm.2023.02.040.
13 P. Afzali, E. Gibertini and L. Magagnin, Improved plating/stripping in anode-free lithium metal batteries through electrodeposition of lithiophilic zinc thin films,

Electrochim. Acta, 2024, **488**, 144190, DOI: 10.1016/j.electacta.2024.144190.

14 N. Li, T. Jia, Y. Liu, S. Huang, F. Kang and Y. Cao, Rational Engineering of Anode Current Collector for Dendrite-Free Lithium Deposition: Strategy, Application, and Perspective, *Front. Chem.*, 2022, **10**, 884308, DOI: 10.3389/fchem.2022.884308.

15 P. Molaiyan, M. Abdollahifar, B. Boz, A. Beutl, M. Krammer, N. Zhang, A. Tron, M. Romio, M. Ricci, R. Adelung, A. Kwade, U. Lassi and A. Paolella, Optimizing Current Collector Interfaces for Efficient "Anode-Free" Lithium Metal Batteries, *Adv. Funct. Mater.*, 2024, **34**, 2311301, DOI: 10.1002/adfm.202311301.

16 M. Lei, Z. You, L. Ren, X. Liu and J.-G. Wang, Construction of copper oxynitride nanoarrays with enhanced lithiophilicity toward stable lithium metal anodes, *J. Power Sources*, 2020, **463**, 228191, DOI: 10.1016/j.jpowsour.2020.228191.

17 Y.-X. Song, W.-Y. Lu, Y.-J. Chen, H. Yang, C. Wu, W.-F. Wei, L.-B. Chen and X.-P. Ouyang, Coating highly lithiophilic Zn on Cu foil for high-performance lithium metal batteries, *Rare Met.*, 2022, **41**(4), 1255–1264, DOI: 10.1007/s12598-021-01811-3.

18 S. Zhang, G. Yang, Z. Liu, S. Weng, X. Li, X. Wang, Y. Gao, Z. Wang and L. Chen, Phase Diagram Determined Lithium Plating/Stripping Behaviors on Lithiophilic Substrates, *ACS Energy Lett.*, 2021, **6**, 4118–4126, DOI: 10.1021/acsenergylett.1c02127.

19 J. Jiang, X. Hu, S. Lu, C. Shen, S. Huang, X. Liu, Y. Jiang, J. Zhang and B. Zhao, Construction of lithophilic solid electrolyte interfaces with a bottom-up nucleation barrier difference for low-N/P ratio Li-metal batteries, *Energy Storage Mater.*, 2023, **54**, 885–894, DOI: 10.1016/j.ensm.2022.11.022.

20 Z. Ni, D. Yang, Y. Wang, W. Yang, B. Deng, J. Hou, Y. Zhang, X. Li and Y. Zhang, The effect of alloy type of lithophilic Cu-Sn interface layer on the deposition/stripping behavior of lithium metal anode, *J. Alloys Compd.*, 2022, **906**, 164307, DOI: 10.1016/j.jallcom.2022.164307.

21 H. E. Kang, J. Ko, S. G. Song and Y. S. Yoon, Recent progress in utilizing carbon nanotubes and graphene to relieve volume expansion and increase electrical conductivity of Si-based composite anodes for lithium-ion batteries, *Carbon*, 2024, **219**, 118800, DOI: 10.1016/j.carbon.2024.118800.

22 Q. Tan, Z. Kong, X. Guan, L. Y. Zhang, Z. Jiao, H. C. Chen, G. Wu and B. Xu, Hierarchical zinc oxide/reduced graphene oxide composite: preparation route, mechanism study and lithium ion storage, *J. Colloid Interface Sci.*, 2019, **548**, 233–243, DOI: 10.1016/j.jcis.2019.04.041.

23 C. Zhao, S. Xiong, H. Li, Z. Li, C. Qi, H. Yang, L. Wang, Y. Zhao and T. Liu, A dendrite-free composite Li metal anode enabled by lithiophilic Co, N codoped porous carbon nanofibers, *J. Power Sources*, 2021, **483**, 229188, DOI: 10.1016/j.jpowsour.2020.229188.

24 S. Sen Chi, Q. Wang, B. Han, C. Luo, Y. Jiang, J. Wang, C. Wang, Y. Yu and Y. Deng, Lithiophilic Zn Sites in Porous CuZn Alloy Induced Uniform Li Nucleation and Dendrite-free Li Metal Deposition, *Nano Lett.*, 2020, **20**, 2724–2732, DOI: 10.1021/acs.nanolett.0c00352.

25 T. Wang, Y. Xiao, S. Tang, W. Xiang and J. S. Yu, Unlocking Quasi-Solid-State Anode-Free Zinc MetalBatteries Through Robust Bilayer Interphase Engineering, *Adv. Energy Mater*, 2025, 2500430, DOI: 10.1002/aenm.202500430.

26 Q. Chen, Y. Yang, H. Zheng, Q. Xie, X. Yan, Y. Ma, L. Wang and D. L. Peng, Electrochemically induced highly ion conductive porous scaffolds to stabilize lithium deposition for lithium metal anodes, *J. Mater. Chem. A*, 2019, **7**, 11683–11689, DOI: 10.1039/c9ta01834d.

27 P. Afzali, E. Gibertini and L. Magagnin, Improved plating/stripping in anode-free lithium metal batteries through electrodeposition of lithiophilic zinc thin films, *Electrochim. Acta*, 2024, **488**, 144190, DOI: 10.1016/j.electacta.2024.144190.

28 Y. Lai, T. Yang, Y. Yang, W. Li, Y. Xie, S. Cheng, L. Qiao and X. Wang, A lithiophilic and conductive interlayer for dendrite-free lithium metal anodes, *Chem. Eng. J.*, 2023, **462**, 142223, DOI: 10.1016/j.cej.2023.142223.

29 Y. X. Zhan, P. Shi, X. X. Ma, C. Bin Jin, Q. K. Zhang, S. J. Yang, B. Q. Li, X. Q. Zhang and J. Q. Huang, Failure Mechanism of Lithiophilic Sites in Composite Lithium Metal Anode under Practical Conditions, *Adv. Energy Mater.*, 2022, **12**, 210329, DOI: 10.1002/aenm.202103291.

30 S. Sen Chi, Q. Wang, B. Han, C. Luo, Y. Jiang, J. Wang, C. Wang, Y. Yu and Y. Deng, Lithiophilic Zn Sites in Porous CuZn Alloy Induced Uniform Li Nucleation and Dendrite-free Li Metal Deposition, *Nano Lett.*, 2020, **20**, 2724–2732, DOI: 10.1021/acs.nanolett.0c00352.

31 C. Maignan, J. G. Alauzun, E. Flahaut, L. Monconduit and B. Boury, Graphene oxide composites: a versatile material used as protective layer, solid-state electrolyte, and gel electrolyte in metal batteries, *Chem. Eng. J.*, 2024, **485**, 149616, DOI: 10.1016/j.cej.2024.149616.

32 D. Wang, J. Guo, C. Cui, J. Ma and A. Cao, Controllable synthesis of CNT@ZnO composites with enhanced electrochemical properties for lithium-ion battery, *Mater. Res. Bull.*, 2018, **101**, 305–310, DOI: 10.1016/j.materresbull.2018.01.052.

33 D. Wu, H. Wu, Y. Niu, C. Wang, Z. Chen, Y. Ouyang, S. Wang, H. Li, L. Chen and L. Y. Zhang, Controllable synthesis of zinc oxide nanoparticles embedded holey reduced graphene oxide nanocomposite as a high-performance anode for lithium-ion batteries, *Powder Technol.*, 2020, **367**, 774–781, DOI: 10.1016/j.powtec.2020.04.046.

34 O. F. Abraham, V. S. Aigbodion, E. C. Ejiogu and U. C. Ogbuefi, Rice husk derived graphene and zinc oxide composite anode for high reversible capacity lithium-ion batteries, *Diam. Relat. Mater.*, 2022, **123**, 108885, DOI: 10.1016/j.mee.2013.12.029.

35 M. O. Guler, T. Cetinkaya, U. Tocoglu and H. Akbulut, Electrochemical performance of MWCNT reinforced ZnO anodes for Li-ion batteries, *Microelectron. Eng.*, 2014, **118**, 54–60, DOI: 10.1016/j.mee.2013.12.029.

36 P. Fan, H. Liu, L. Liao, J. Fu, Z. Wang, G. Lv, L. Mei, H. Hao, J. Xing and J. Dong, Flexible and high capacity lithium-ion

battery anode based on a carbon nanotube/electrodeposited nickel sulfide paper-like composite, *RSC Adv.*, 2017, **7**, 49739–49744, DOI: **10.1039/c7ra08239h**.

37 J. Ma, J. Yang, C. Wu, M. Huang, J. Zhu, W. Zeng, L. Li, P. Li, X. Zhao, F. Qiao, Z. Zhang, D. He and S. Mu, Stabilizing nucleation seeds in Li metal anode *via* ion-selective graphene oxide interfaces, *Energy Storage Mater.*, 2023, **56**, 572–581, DOI: **10.1016/j.ensm.2023.01.045**.

38 M. C. Schulze, R. M. Belson, L. A. Kraynak and A. L. Prieto, Electrodeposition of Sb/CNT composite films as anodes for Li- and Na-ion batteries, *Energy Storage Mater.*, 2020, **25**, 572–584, DOI: **10.1016/j.ensm.2019.09.025**.

39 Z. T. Wondimkun, T. T. Beyene, M. A. Weret, N. A. Sahalie, C.-J. Huang, B. Thirumalraj, B. A. Jote, D. Wang, W.-N. Su, C.-H. Wang, G. Brunklaus, M. Winter and B.-J. Hwang, Binder-free ultra-thin graphene oxide as an artificial solid electrolyte interphase for anode-free rechargeable lithium metal batteries, *J. Power Sources*, 2020, **450**, 227589, DOI: **10.1016/j.jpowsour.2019.227589**.

40 M. Dirican, M. Yanilmaz, K. Fu, Y. Lu, H. Kizil and X. Zhang, Carbon-enhanced electrodeposited SnO_2/carbon nanofiber composites as anode for lithium-ion batteries, *J. Power Sources*, 2014, **264**, 240–247, DOI: **10.1016/j.jpowsour.2014.04.102**.

41 Y. Lai, T. Yang, Y. Yang, W. Li, Y. Xie, S. Cheng, L. Qiao and X. Wang, A lithiophilic and conductive interlayer for dendrite-free lithium metal anodes, *Chem. Eng. J.*, 2023, **462**, 142223, DOI: **10.1016/j.cej.2023.142223**.

42 D. Cai and M. Song, Recent advance in functionalized graphene/polymer nanocomposites, *J. Mater. Chem.*, 2010, **20**, 7906–7915, DOI: **10.1039/c0jm00530d**.

43 K. Flores, C. Valdes, D. Ramirez, T. M. Eubanks, J. Lopez, C. Hernandez, M. Alcoutlabi and J. G. Parsons, The effect of hybrid zinc oxide/graphene oxide (ZnO/GO) nano-catalysts on the photocatalytic degradation of simazine, *Chemosphere*, 2020, **259**, 127414, DOI: **10.1016/j.chemosphere.2020.127414**.

44 M. Genovese, A. J. Louli, R. Weber, R. J. Sanderson, M. B. Johnson and J. R. Dahn, Combinatorial Methods for Improving Lithium Metal Cycling Efficiency, *J. Electrochem. Soc.*, 2018, **165**, A3000–A3013, DOI: **10.1149/2.0401813jes**.

45 J. Su, X. Yin, H. Zhao, H. Yang, D. Yang, L. He, M. Wang, S. Jin, K. Zhao, Y. Wang and Y. Wei, Temperature-Dependent Nucleation and Electrochemical Performance of Zn Metal Anodes, *Nano Lett.*, 2022, **22**, 1549–1556, DOI: **10.1021/acs.nanolett.1c04353**.

46 S. Bhoyate, S. Mhin, J. Jeon, K. Park, J. Kim and W. Choi, Stable and High-Energy-Density Zn-Ion Rechargeable Batteries Based on a MoS_2-Coated Zn Anode, *ACS Appl. Mater. Interfaces*, 2020, **12**, 27249–27257, DOI: **10.1021/acsami.0c06009**.

47 C. Huang, X. Zhao, S. Liu, Y. Hao, Q. Tang, A. Hu, Z. Liu and X. Chen, Stabilizing Zinc Anodes by Regulating the Electrical Double Layer with Saccharin Anions, *Adv. Mater.*, 2021, **33**, 2100445, DOI: **10.1002/adma.202100445**.

48 F. Zhu, J. Wang, Y. Zhang, H. Tu, X. Xia, J. Zhang, H. He, H. Lin and M. Liu, Low-Temperature Lithium Metal Batteries Achieved by Synergistically Enhanced Screening Li^+ Desolvation Kinetics, *Adv. Mater.*, 2025, **37**, 2411601, DOI: **10.1002/adma.202411601**.

49 J. Wang, J. Zhang, S. Duan, L. Jia, Q. Xiao, H. Liu, H. Hu, S. Cheng, Z. Zhang, L. Li, W. Duan, Y. Zhang and H. Lin, Lithium Atom Surface Diffusion and Delocalized Deposition Propelled by Atomic Metal Catalyst toward Ultrahigh-Capacity Dendrite-Free Lithium Anode, *Nano Lett.*, 2022, **22**, 8008–8017, DOI: **10.1021/acs.nanolett.2c02611**.

50 J. Zhang, C. You, H. Lin and J. Wang, Electrochemical Kinetic Modulators in Lithium–Sulfur Batteries: From Defect-Rich Catalysts to Single Atomic Catalysts, *Energy Environ. Mater.*, 2022, **5**, 731–750, DOI: **10.1002/eem2.12250**.

51 J. Wang, L. Li, H. Hu, H. Hu, Q. Guan, M. Huang, L. Jia, H. Adenusi, K. V. Tian, J. Zhang, S. Passerini and H. Lin, Toward Dendrite-Free Metallic Lithium Anodes: From Structural Design to Optimal Electrochemical Diffusion Kinetics, *ACS Nano*, 2022, **16**, 17729–17760, DOI: **10.1021/acsnano.2c08480**.

52 K. Natarajan, S.-H. Wu, Y.-S. Wu, J.-K. Chang, R. Jose and C.-C. Yang, Tuning intrinsic lithiophilicity of copper foil to improve electrochemical performance of anode-free Li metal battery, *J. Energy Storage*, 2024, **84**, 110880, DOI: **10.1016/j.est.2024.110880**.

53 A. K. Mishra, J. Parmar and I. Mukhopadhyay, Comprehensive review on nucleation, growth, and suppression of lithium dendrites in lithium anode batteries, *J. Energy Storage*, 2024, **87**, 111421, DOI: **10.1016/j.est.2024.111421**.

54 B. Yu, T. Tao, S. Mateti, S. Lu and Y. Chen, Nanoflake Arrays of Lithiophilic Metal Oxides for the Ultra-Stable Anodes of Lithium-Metal Batteries, *Adv. Funct. Mater.*, 2018, **28**, 1803023, DOI: **10.1002/adfm.201803023**.

55 W. Zhu, J. Zhao and X. Tao, MoS_2-carbon based nanocomposites as anodes for lithium-ion batteries: a review, *J. Energy Storage*, 2024, **84**, 110934, DOI: **10.1016/j.est.2024.110934**.

56 G. Ge, Y. Wu, E. van der Heide, Z. Chen, J. Zhu and X. Zhuang, Carbon nanomaterials-constructed electrodes for rechargeable metal-ion batteries, *J. Energy Storage*, 2024, **90**, 111900, DOI: **10.1016/j.est.2024.111900**.

57 C. Zhou, A. J. Samson, M. A. Garakani and V. Thangadurai, Communication—Anode-Free Lithium Metal Batteries: A Case Study of Compression Effects on Coin Cell Performance, *J. Electrochem. Soc.*, 2021, **168**, 060532, DOI: **10.1149/1945-7111/ac0998**.

58 X. Shu, W. Yang, B. Yang, K. Wei, K. Punyawudho and C. Liu, Research on EIS characterization and internal morphological changes of LIBs during degradation process, *Eng. Failure Anal.*, 2024, **155**, 107764, DOI: **10.1016/j.engfailanal.2023.107764**.